Adjoint-Based Simultaneous State and Parameter Estimation in an Arctic Sea Ice-Ocean Model using MITgcm (c63m)

Guokun Lyu[12], Longjiang Mu[3], Armin Koehl[4] , Ruibo Lei[1*], Xi Liang[5], and Chuanyu Liu[6]

[1]Key Laboratory for Polar Science, Polar Research Institute of China, Ministry of Natural Resources, Shanghai, 200136, China
[2]Shanghai Key Laboratory of Polar Life and Environment Sciences, School of Oceanography, Shanghai Jiao Tong University, Shanghai, 200230, China
[3]Laoshan Laboratory, Qingdao, 266100, China
[4]Center for Earth System Research and Sustainability (CEN), Universität Hamburg, Hamburg, 54662, Germany
[5]Key Laboratory of Marine Hazards Forecasting, National Marine Environmental Forecasting Center, Ministry of Natural Resources, Beijing, 100081,China
[6]Key Laboratory of Ocean Observation and Forecasting, and Key Laboratory of Ocean Circulation and Waves, Institute of Oceanology, Chinese Academy of Sciences, Qingdao, 266000, China

Corresponding to: Ruibo Lei (leiruibo@pric.org.cn)

Abstract. Parameters in sea ice-ocean coupled models greatly affect the simulated evolution of the ocean and sea ice, and are typically tuned to bring the model state close to observations. Using an adjoint method, spatiotemporally varying parameters of an Arctic sea ice-ocean coupled model are optimized simultaneously with the initial conditions and atmospheric forcing by assimilating satellite and in-situ observations. The assimilation results show that the joint state and parameter estimation (SPE) substantially improves the sea ice concentration simulations. Particularly in October, when the ocean surface starts to refreeze, SPE reduces the lead closing parameter H_o (which determines the minimum ice thickness formed in the open water), thereby increasing the sea ice growth and facilitating the seasonal rapid sea ice recovery in the Arctic's Pacific sector. Comparisons with sea ice thickness observations from the moored upward-looking sonars and Ice Mass Balance buoys demonstrate that incorporating optimized model parameters into the coupled model also leads to better sea ice thickness estimation. Given that the optimal set of sea ice parameters may evolve alongside the thinning of Arctic sea ice, the adjoint-based SPE scheme has the potential to more accurately reconstruct the histical Arctic ocean and sea ice changes covering the satellite era, supporting research on Arctic sea ice and ocean variability.

带格式的: 字体: (默认) Times New Roman, 10 磅, 图案: 清除

删除的内容: Overall, the adjoint-based SPE scheme has the potential to more accurately reproduce the Arctic ocean and sea ice state and will be appled to produce a new Arctic sea ice-ocean reanalysis dataset.

1 Introduction

In climate models, parameterizations are widely used to simulate the effects of unresolved processes on large-scale state variables. The parameters in these parameterizations significantly affect model simulations across various spatial and temporal scales (e.g., Mauritsen et al., 2012; Murphy et al., 2004). This is particularly important for the Arctic system, where observations are extremely scarce, and the ocean and sea ice states are undergoing rapid changes.

Most model parameters cannot be measured directly. Usually, a globally uniform value for individual parameters is assumed as the default in parameterization schemes. When incorporated into complex climate models, sensitive parameters are usually further adjusted to bring the model's climatology closer to observed state (e.g., Hourdin et al., 2017; Mauritsen et al., 2012). The underlying assumption is that these sensitive parameters determine the model's climatology and variations. Over the past decades, manual (e.g., Mauritsen et al., 2012) and automatic tuning (e.g., Jackson et al., 2008; Williamson et al., 2013; Yang et al., 2013) methods have been developed to optimize a number of sensitive parameters (on the order of 10). In addition, data assimilation techniques, including ensemble Kalman filters (Annan et al., 2005; Massonnet et al., 2014; Wu et al., 2012) and the adjoint method (Liu et al., 2012; Lyu et al., 2018), have been tested for optimizing spatiotemporally varying parameters with large dimensions.

In sea ice models, parameters significantly affect the sea ice's seasonal and interannual evolutions, as well as the heat, freshwater, and momentum budgets of the sea ice-ocean-atmosphere system (e.g., Kim et al., 2006; Uotila et al., 2012; Nie et al., 2023). Similar to climate models, these parameters are manually tuned through a trial-and-error process to match the historical sea ice state (e.g., Hibler, 1979; Miller et al., 2005). Automated parameter estimation methods, such as genetic algorithms (Sumata et al., 2019), ensemble Kalman filters (Massonnet et al., 2014), and the adjoint method (Lu et al., 2021; Lyu et al., 2018; Panteleev et al., 2020), are applied to optimize sensitive parameters using satellite sea ice observations. More recently, machine learning (e.g., Bretherton et al., 2022; Horvat & Roach, 2022; Kochkov et al., 2024) has been applied to develop the sub-grid parameterizations using high-resolution model simulations and reanalysis datasets. However, improvements in observed variables often come with detrimental effects on the other variables or in some regions. For instance, Massonnet et al. (2014) reported that the improvements in sea ice speed were accompanied by an overestimation of winter ice areal outflow through the Fram Strait.

Several factors are likely responsible for these detrimental effects. First, model parameters represent only parts of the model's uncertain inputs, and they may be over-adjusted to compensate for errors in the other uncertain inputs. For instance, Miller et al. (2005) suggested that optimal parameters likely compensate for deficiencies in atmospheric forcing. Therefore, it is necessary to optimize the model's uncertain inputs simultaneously. Second, the sensitivities of the sea ice state to parameter perturbations show distinct spatiotemporal patterns (Kim et al., 2006; Miller et al., 2005), suggesting that allowing optimized parameters to vary geographically and temporally is likely to further improve model performance. Additionally, it is necessary to use more comprehensive Arctic ocean and sea ice observations to constrain model parameters and the other uncertain inputs.

In the framework of data assimilation, simultaneous state and parameter estimation (SPE) can be achieved by including spatiotemporally varying parameters in the set of control variables (e.g., Hu et al., 2010; Liu et al., 2012; Wu et al., 2012; Zhang, 2011). Since initial conditions typically exert significant influences on short timescales within the Earth system, while parameters are more important on longer timescales (e.g., Branstator & Teng, 2010),

72 constructing an error propagation model to project model-data misfits onto both initial conditions and parameters is

73 challenging. Using an ensemble Kalman filter with a short assimilation window (within the predictability limit of the

74 chaotic system), Zhang (2011) proposed to optimize the initial state first until the model-data misfits reach a quasi-

75 equilibrium, where the parameter errors dominate; then they optimized the model parameters to reduce residual errors.

76 Liu et al. (2012) used an adjoint model to project the model-data misfits over a large assimilation window onto initial

77 conditions, atmospheric forcing, and eddy mixing parameters.

78   Applications of SPE in ocean models (Liu et al., 2012) and coupled climate models of intermediate complexity

79 (Wu et al., 2012) have demonstrated additional effects on mitigating model bias and improving prediction accuracy.

80 However, to date, parameter estimation (Lu et al., 2021; Panteleev et al., 2020) and state estimation (e.g., Fenty et al.,

81 2017;Forget et al., 2015; Lindsay & Zhang, 2006; Lyu et al., 2021b; Mu et al., 2018; Nguyen et al., 2021; Liu et al.,

82 2018) are performed separately in the sea ice-ocean coupled model. Given the rapid thinning of the Arctic sea ice and

83 its extremely strong spatial heterogeneity, it is necessary to have parameters that vary spatiotemporally in response to

84 the changing climate background. Therefore, we developed SPE in a sea ice-ocean coupled model and investigated its

85 potential effects by assimilating satellite and in-situ measurements.

86   This paper is organized as follows. In Section 2, we introduce the coupled sea ice-ocean assimilation system,

87 including the model configuration, the parameters being adjusted, as well as the assimilated and independent

88 observations. Section 3 briefly evaluates the parameter sensitivities and accuracy of the adjoint model based on the

89 tangent linear model. Section 4 discusses the added effects of SPE. Finally, we summarize this study in Section 5.

90 **2 Methodology**

91 **2.1 The Pan-Arctic Ocean and Sea Ice Assimilation System**

92   The sea ice-ocean coupled assimilation system is based on the adjoint method (4D-Var in operational oceanic

93 and meteorological forecasting communities) from the Estimating the Circulation and Climate of the Ocean (ECCO)

94 project. It employs the Massachusetts Institute of Technology general circulation model (MITgcm, Marshall et al.,

95 1997) coupled with a zero-layer dynamic and thermodynamic sea ice model (Hibler, 1979; Hibler, 1980; Losch et al.,

96 2010). The sea ice dynamics are based on a viscous-plastic rheology and solved using a line successive over-relaxation

97 algorithm (Zhang & Hibler, 1997).

98   The adjoint of the sea ice-ocean coupled model is generated using the Transformation of Algorithms in Fortran

99 (Giering & Kaminski, 1998; Heimbach et al., 2010). In previous studies, due to persistent instability issues, the adjoint

100 of the sea ice dynamics was usually excluded (Fenty & Heimbach, 2013; Fenty et al., 2017; Nguyen et al., 2021) or

101 simplified to the adjoint of free-drift sea ice dynamics (Koldunov et al., 2017; Lyu et al., 2021a; Lyu et al., 2021b) in

102 assimilation experiments. Recently, Lyu et al. (2023) incorporated and approximated the adjoint of viscous-plastic sea

103 ice dynamics. In this study, we use the same model configuration as Lyu et al. (2023). Horizontally, we use a

104 curvilinear grid with a resolution of $12-18$ km. Vertically, we have 50 z-levels with layer thickness ranging from 10

105 m at the surface to 456 m in the deep ocean. In addition, we further developed the adjoint model to jointly estimate

106 the state and spatiotemporally varying parameters, and evaluated the added effects by comparing with the results in
107 Lyu et al. (2023).

108   The adjoint method minimizes a quadratic function (J) iteratively by adjusting the control variables (C) to bring
109 the model simulation closer to available observations:

110 $$J(C) = \sum_{t=1}^{T1}[y(t) - E(t)x(t)]^T R^{-2}[y(t) - E(t)x(t)] + \Delta C B^{-2} \Delta C^T \qquad (1)$$

111   The first term on the right-hand side computes the "distance" between observations (x) and corresponding model-
112 simulated variables (y) over a long period (one year in this study). The model-data misfits are normalized by their
113 prior error (R). E interpolates the model state to the observations. Values of R for different observation types are
114 introduced in Section 2.2.

115   The second term on the right-hand side measures the magnitude of the adjustments to the control variables (ΔC)
116 and B^{-2} is the background error covariance. In the 3D-Var and 4D-Var system with short assimilation windows (on
117 the order of days), covariance matrix B^{-2} is critical for filling in observational gaps and achieving the multivariate
118 adjustments to initial conditions (Li et al., 2008; Weaver & Mirouze, 2013). However, on longer timescales (several
119 months to years), this is no longer necessary because the advection and diffusion in the adjoint model transport
120 information about model-data misfits to locations without observations and to unobserved variables. Therefore, for
121 simplicity, we use a diagonal B matrix, and the second term on the right-hand side of equation (1) is simplified to $\frac{\Delta C^2}{\sigma^2}$,
122 where σ represent the corresponding errors. As this term increases quadratically with ΔC, it limits the magnitude of
123 adjustments during optimization.

124   In addition to the initial oceanic temperature and salinity, sea ice concentration (SIC), sea ice thickness (SIT),
125 and daily atmospheric state, which includes 2-m air temperature, 2-m specific humidity, precipitation rate, 10-m wind
126 vectors, downward longwave radiation, and net shortwave radiation, we further include 13 spatiotemporally varying
127 model parameters (see Table 1) in the control variables. These parameters vary by geographic location and on a daily
128 basis. The uncertainties of 13 parameters are not precisely known; their error distributions are assumed to be Gaussian,
129 with standard deviations of 20% of their default values.

130   The assimilation system iteratively minimizes the cost function J using a quasi-Newton algorithm (Gilbert &
131 Lemaréchal, 2006) and gradient information $\frac{\partial J}{\partial C}$. The optimization stops when the cost function can no longer be
132 reduced. The adjoint of the ocean-sea ice coupled model is used to compute $\frac{\partial J}{\partial C}$ which has dimensions of 10^8. To ensure
133 the stability of the adjoint model over a one-year period, modifications to the adjoint codes are handled carefully.
134 Details are provided in Lyu et al. (2023). The accuracy of the adjoint model is presented in Section 3.

135 **2.2 The Assimilation Experiments and the Control Variables**
136   Two assimilation experiments and one control run were performed to examine the additional effects of SPE. The
137 initial condition for January 1, 2012, is taken from the Arctic sea ice-ocean reanalysis by Lyu et al. (2021b), which
138 used the same model configuration as in this study. We take the forward simulation at iteration 0 as the control run
139 (CTRL). The two assimilation experiments differ in their choice of control variables. In the first assimilation
140 experiment, only the initial conditions and atmospheric forcings are adjusted (hereinafter named opti-SE). In the

141 second assimilation experiment, we further include 13 spatiotemporally varying model parameters (see Table 1 for

142 details) in the control variables (hereinafter named opti-SPE). Based on a previous study with a similar sea ice module

143 (Sumata et al., 2019) and our sensitivity experiments, we identified these 13 sea ice parameters, which have

144 considerable impact on sea ice properties. To prevent over-adjustments of the parameters, which may result in model

145 instability, we further set upper and lower bounds for individual parameters in the model (Table 1).

146 Table 1. The sea ice model parameters applied as additional control variables for optimization

Parameters	Description	Default Values	Lower/Upper bounds
α_{wice}	Albedo of melting ice	0.66	0.50, 0.95
α_{dice}	Ice albedo	0.75	0.50, 0.95
α_{wsnow},	Albedo of melting snow	0.71	0.50, 0.95
α_{dsnow}	Snow albedo	0.83	0.50, 0.95
$Cond_{ice}$	Ice conductivity (W·m^{-1}·K^{-1})	2.17	1.50, 3.00
$Cond_{snow}$	Snow conductivity (W·m^{-1}·K^{-1})	0.31	0.15, 0.40
C_{d_wind}	Wind-ice drag coefficient	2.0×10^{-3}	1.0×10^{-3}, 5.0×10^{-3}
C_{d_water}	Water-ice drag coefficient	5.5×10^{-3}	1.0×10^{-3}, 10.0×10^{-3}
H_o	Lead closing parameter, which determines the minimum sea ice thickness formed in open water (m)	0.5	0.03, 1.0
$P*$	Ice compressive strength constant (N m^{-2})	2.8×10^{4}	1.0×10^{4}, 5.0×10^{4}
$C*$	Ice strength decay constant	-20.0	-30.0, -5.0
Es	Eccentricity of the yield curve describing the viscous-plastic rheology	2.0	1.5, 2.3
F_T	Friction velocity for ice-ocean heat flux (m s^{-1})	0.88×10^{-3}	0.4×10^{-3}, 1.2×10^{-3}

147

148 **2.2 Assimilated Observations**

149 We assimilate both satellite and in-situ observations (listed in Table 2). In the assimilation process, the

150 observations and their errors must be provided beforehand. Errors for these types of observations are described in

151 previous studies (Lyu et al., 2023).

152 Altimeter along-track L3 sea surface heights anomalies (SLA) are assimilated with observational errors of 3 cm.

153 Gridded sea surface temperature (SST) data for open waters and their associated errors are based on optimally

154 interpolated microwave and infrared data from the Remote Sensing System (Gentemann et al., 2004). Subsurface

155 oceanic temperature and salinity data are based on the EN4 dataset (Good et al., 2013). Observational errors of

156 temperature and salinity (T&S) profiles are depth-dependent, ranging from ~0.6 °C and ~0.3 PSU at the surface to

157 ~0.02 °C and ~0.02 PSU in the deep ocean. The World Ocean Atlas 2018 (WOA18) climatology is also assimilated

158 to reduce biases in ocean temperature and salinity, with their prior errors set to five times those of the in-situ profiles.

159 Since we interpolate the WOA18 to the finer model grids, which implicitly increases the number of the observations,

160 we reduce the weight of temperature and salinity climatology cost components by multiplying by a factor of 0.04.

161 We assimilate the SIC observations from the Special Sensor Microwave/Imager (SSM/I) and ARTIST Sea Ice

162 (ASI) algorithm (Kaleschke et al., 2001; Spreen et al., 2008). This dataset does not provide observational error

163 estimates. In data assimilation studies, the observational errors should consist of representation and instrumental errors.

164 Considering larger SIC errors near coastlines due to reduced accuracy in the SIC product and poor representation of

165 landfast ice in the model (Fenty & Heimbach, 2013), we set the representation errors to 15% within 50 km of the

166 coastline and 10% in other areas. Additionally, considering the dependence of SIC errors on the absolute value of SIC

167 (Chen et al., 2023), we multiply the representation errors by factors of 0.85, 1.20, 1.10, and 1.00 for observed SIC

168 ranges of 0%, < 15%, 15% − 25%, and > 25%, respectively.

169   Satellite SIT observations are based on the merged CryoSat-2 and SMOS product (CS2SMOS), which includes

170 observational error estimates (Ricker et al., 2017). The SIT in this dataset represents the mean SIT over 25 km×25 km

171 areas but excludes open waters. Note that since the model simulates the grid-mean SIT (SIT×SIC), we convert the

172 model-simulated grid-mean SIT to the mean SIT over ice-covered regions before comparing it against the satellite

173 SIT observations in the cost function. Satellite sea ice drift (SID) data are derived from the Ocean & Sea Ice Satellite

174 Application Facility (OSISAF, https://osi-saf.eumetsat.int) product at a resolution of 62.5 km, which applies a

175 continuous maximum cross-correlation method to track the sea ice displacements over a 48-hour period from

176 sequences of satellite images (Lavergne et al., 2010). The errors are dominated by satellite resolution (10–15 km), and

177 are set to 10 km every 2 days (~0.06 m s^{-1}).

178 Table 2. Assimilated Observations.

Observations[1]	Resolution	Number	Source	Reference
SLA	7.0 km	7.6×10^5	http://marine.copernicus.eu	(Pujol et al., 2016; Taburet et al., 2019)
SST	25.0 km	2.0×10^7	https://data.remss.com/SST/daily/mw_ir/v05.1/netcdf/, (last access: 13 April 2025)	(Gentemann et al., 2004)
T&S	–	5.0×10^5	https://www.metoffice.gov.uk/hadobs/en4/download-en4-2-2.html, (last access: 13 April 2025)	(Good et al., 2013)
SIC	25.0 km	3.6×10^7	https://thredds.met.no/thredds/catalog/osisaf/met.no/reprocessed/ice/conc_450a_files/catalog.html (last access: 13 April 2025)	(Lavergne et al.,2019)
SIT	25.0 km	8.9×10^6	https://spaces.awi.de/display/CS2SMOS/CryoSat-SMOS+Merged+Sea+Ice+Thickness (last access: 13 April 2025)	(Ricker et al., 2017)
SID	62.5 km	5.8×10^5	https://thredds.met.no/thredds/catalog/osisaf/met.no/ice/drift_lr/merged/catalog.html (last access: 13 April 2025)	(Lavergne et al., 2010)
WOA18	1°	2.9×10^7	https://www.ncei.noaa.gov/access/world-ocean-atlas-2018/ (last access: 13 April 2025)	(Locarnini et al., 2018; Zweng et al., 2018)

179 [1] SLA sea surface height anomaly, SST sea surface temperature, T&S temperature and salinity profiles from EN4
180 datasets, SIC sea ice concentration, SIT sea ice thickness, SID sea ice drift, WOA18 World Ocean Atlas 2018

181 **2.3 Independent Observations**

182   Independent sea ice observations are used to validate the assimilation results. The observations can be categorized

183 into two groups: 1) single-point measurements, which include sea ice variables within a small area or at specific sites,

184 such as SIT or snow depth from the Ice Mass Balance buoys (IMBs) and ice draft from moored upward-looking sonars

185 (ULSs); 2) gridded measurements, such as remote sensing products. These two types of measurements are not fully

186 consistent, especially in regions with strong spatial heterogeneity of sea ice and prevalent ice dynamic processes.
187 Nevertheless, we use these data to validate and cross-validate the assimilation results and gridded SIT observations,
188 identifying potential discrepancies among the assimilated datasets, the numerical model, and the point observations.

189 **2.3.1 Ice Mass Balance Buoy**

190 IMBs are ice-based observing systems that measure the evolution of snow and sea ice growth and ablation, as
191 well as vertical temperature profiles through the snow, ice, and upper ocean along ice drift trajectories. It uses two
192 acoustic sensors to measure the ice surface and bottom. SIT is derived from the distance between ice surface and
193 bottom. The errors in measurements of the ice surface and bottom by each acoustic sounders are $\pm$ 5mm (Richter-
194 Menge et al., 2006). IMBs are deployed on thick and level ice floes to achieve relatively long measurement periods.
195 It must be acknowledged that directly comparing this point measurements of SIT with gridded SIT is not
196 straightforward. Thus, we also compare the mean SIT bias and temporal changes in SIT along the drifting trajectories.
197 Compared to the satellite or helicopter-based altimeter observations, the IMB observations can effectively characterize
198 the thermodynamic thickening of sea ice (Koo et al., 2021; von Albedyll et al., 2022).

199 **2.3.2 International Arctic Buoy Programme**

200 The International Arctic Buoy Programme (IABP, https://iabp.apl.uw.edu/index.html) collects ice-based drifting
201 buoys from various organizations. Most of these buoys also monitor sea level pressure and surface air temperature
202 along the ice drift trajectories. In this study, we compute sea ice velocities based on drift trajectories and compare
203 them with the model simulations. For 2012, we selected 23 trajectories with continuous position observations of more
204 than 100 days for model validation.

205 **2.3.3 Mooring measurements from the Beaufort Gyre Exploration Project**

206 Starting from 2003, the Beaufort Gyre Exploration Project (BGEP), based at the Woods Hole Oceanographic
207 Institution (https://www2.whoi.edu/site/beaufortgyre/), deployed ULSs at three locations: M_a, M_b, and M_d (see Figure
208 7). The ULSs measure local sea ice draft with an error of $\pm$ 0.1m (Krishfield et al., 2014). In this study, we use daily-
209 averaged sea ice draft for comparisons. Sea ice drafts are converted to sea ice thickness by multiplying with a factor
210 of 1.1, calculated as ratio between mean seawater density (1024.0 kg m^{-3}) and sea ice density (910.0 kg m^{-3}), assuming
211 no snow on the sea ice (Nguyen et al., 2011).

212 **3 Parameter Sensitivities and Accuracy of the Tangent Linear Approximation**

213 There are two requirements for optimizing model parameters using observations. First, parameter changes within
214 the range of uncertainties have considerable impacts on model simulations. For instance, the SIC changes caused by
215 parameter uncertainties should be larger than observational errors. Second, the error propagation model (the tangent
216 linear model in this study) must accurately reproduce the spatiotemporal error propagations induced by the uncertain
217 model inputs.

218   Here, we adjust each of the 13 model parameters (see Table 1) individually by adding 10% of their default values
219 and integrate the model over 2012. We then evaluate the spatiotemporal changes in SIC normalized by satellite SIC
220 observational errors (e.g., 15%). Normalized SIC changes > 1.0 indicate that the SIC changes caused by 10%
221 parameter perturbations are detectable by satellite observations. As Figure 1 shows, albedos of the dry/wet snow and
222 ice (α_{dsnow}, α_{dice}, α_{wsnow}, α_{wice},) have pronounced impacts on summertime SIC. The wind-ice drag coefficient (Cd_{wind})
223 and ice compressive strength constant (P^*) also exhibit large impacts throughout the year. For the remaining
224 parameters, the normalized SIC changes grow slowly and show little seasonal dependence.
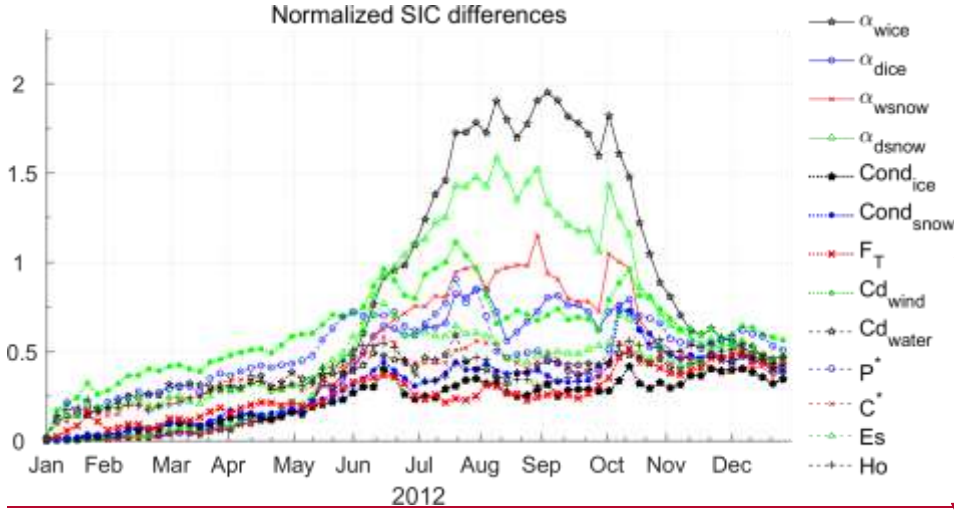
226 **Figure 1. Temporal evolutions of the norm of the SIC differences (normalized by 15% SIC) averaged over the ice-covered**
227 **regions due to the 10% perturbations on the 13 parameters (see the legend and Table 1 for description of the parameters).**

229   The accuracy of the tangent linear approximation is examined using the Taylor expansion. Taking the parameter
230 H_o (lead closing parameter) as an example, we perturb it by $\Delta H_o = 10\% \times H_0$ and evaluate the first-order and higher-
231 order approximations as follows:

232 $\Delta X_1 = M(H_o + \Delta H_o) - M(H_o) = \frac{\partial M}{\partial H} \cdot \Delta H_o + o(\Delta H_o{}^2)$ (2),

233 and $\Delta X_2 = M(H_o - \Delta H_o) - M(H_o) = -\frac{\partial M}{\partial H} \cdot \Delta H_o + o(-\Delta H_o{}^2)$ (3).

234   Here, M is the model operator and X represents the model variables. The linear (first-order) and nonlinear (higher-
235 order) errors can be obtained by $\frac{1}{2}(\Delta X_1 - \Delta X_2)$ and $\frac{1}{2}(\Delta X_1 + \Delta X_2)$. By integrating the tangent linear model with
236 $\Delta H_o = 10\% \times H_0$, we obtain error evolution of the model variables.
237   Although the overall impacts of H_o on SIC do not exceed the SIC observational errors (normalized SIC changes
238 < 1.0; Figure 1) over the one-year period, it exerts substantial impacts on open water during refreezing (Figure 2a).
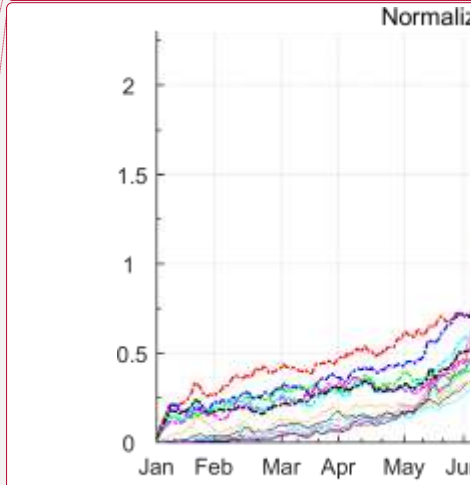
240   Since H_o determines the initial sea ice thickness formed in open water, increasing H_o by 10% will delay the formation

241   of new ice in open water, reducing sea ice coverage across the Arctic Ocean. The signals are dominated by the linear

242   component (Figure 2a), and the nonlinear component is small (Figure 2b). The tangent linear model can reproduce the

243   negative SIC changes very well (Figure 2c).
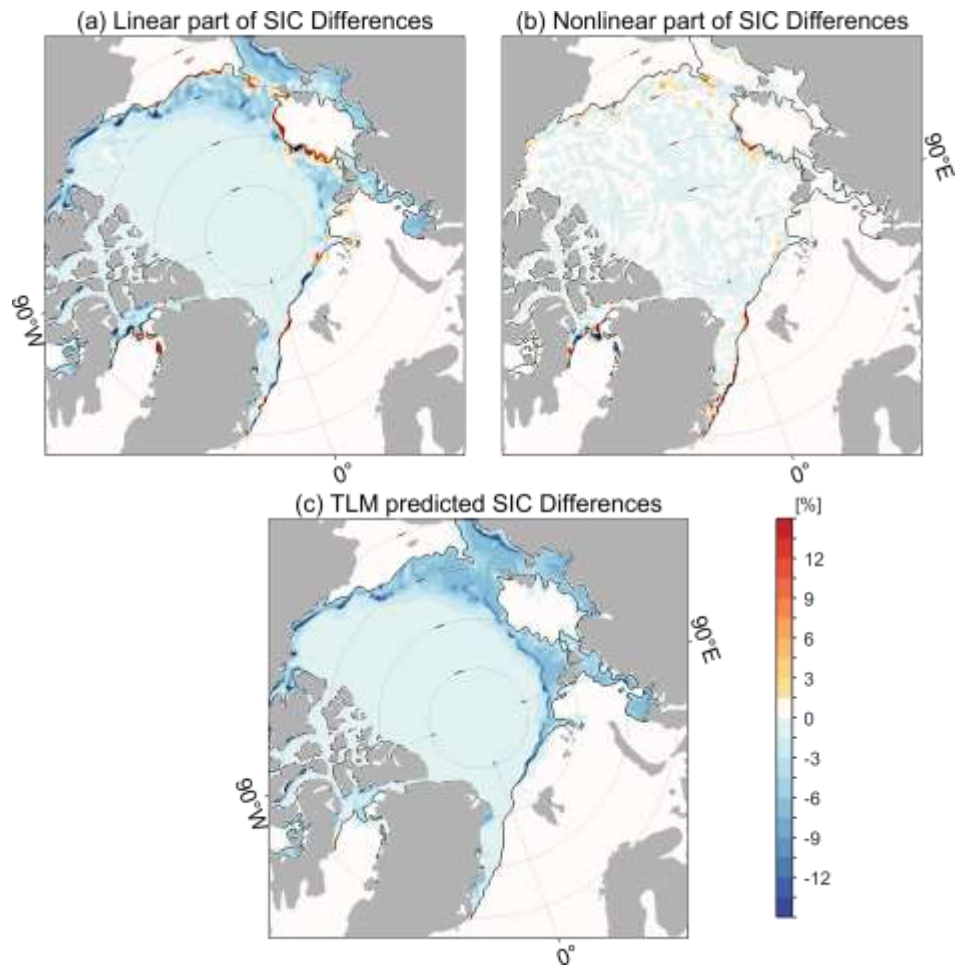
244

245   Figure 2. (a) The linear and (b) nonlinear parts of SIC differences on November 11, 2012 computed using equations (2)-(3).
246   Panel (c) is the corresponding SIC changes predicted by the tangent linear model (TLM). The black lines denote the 15%
247   SIC contour.

248

249   The above analysis demonstrates that the responses of SIC to parameter perturbations are dominated by the linear

250   component, and that the tangent linear model effectively captures the linear component of the error propagation,

251 reproducing both its pattern and amplitude. These results motivate us to further explore the potential of using
252 observations to simultaneously estimate the state and parameters.

253 **4 Evaluation of the Assimilation Results**

254 In this section, we evaluate the impacts of SPE on the estimated sea ice state. Additionally, we compare the two
255 assimilation runs and the control run against independent observations.

256 **4.1 The cost function reduction**

257 The optimization algorithm iteratively reduces the cost function J using the gradients $\frac{\partial J}{\partial c}$. In the opti-SE and opti-
258 SPE, the optimizations stop at iterations 32 and 86, respectively. The cost functions are reduced to 59.8% and 49.3%
259 of their initial values (Figure 3), and the norms of the gradients ($\left|\frac{\partial J}{\partial c}\right|$) are reduced to 10.7% and 9.0%, respectively.

260 Of the assimilated observations, daily SST and SIC contribute to 27.3% and 42.9% of the cost function,
261 respectively, with these proportions reduced to 14.0% and 19.4% in opti-SE and to 10.1% and 13.2% in opti-SPE. For
262 other observations, their cost components are slightly reduced. In the following sections, we focus on improvements
263 in the SIC, SIT, and SID, and evaluate the simulations against independent observations.
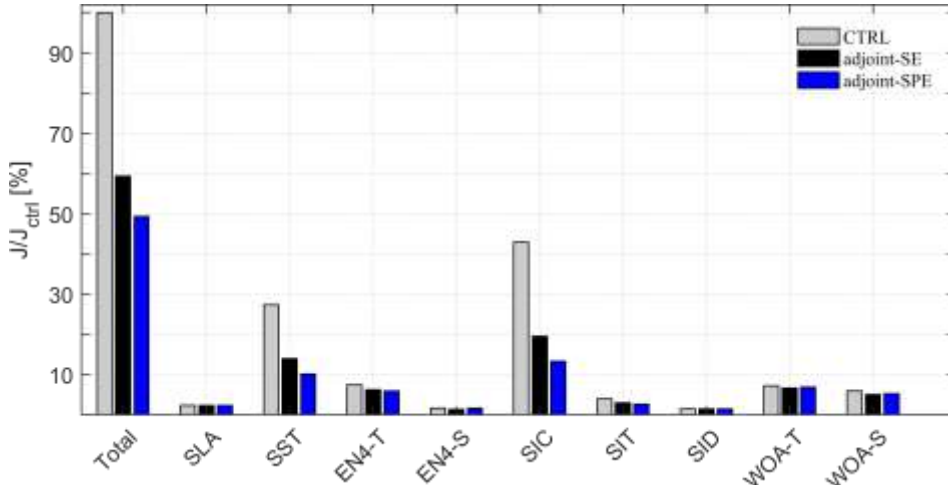
264
265 **Figure 3. The total cost function and individual components normalized by the total cost function in the control run (J$_{ctrl}$).**
266 **Abbreviations: SLA—sea level anomalies, SST—sea surface temperature, EN4-T—EN4 temperature profiles, EN4-**
267 **S—EN4 salinity profiles, SIC—sea ice concentration, SIT—sea ice thickness, SID—sea ice drift velocities; WOA—T and**
268 **WOA—S, climatological temperature and salinity from WOA18 dataset.**

269 **4.2 Improvements on Sea Ice Concentration**

270 In the control run (CTRL), normalized SIC errors grow rapidly during spring, peaking in June. They then decrease
271 from July to September before sharply increasing again in October (grey dotted line with filled circles in Figure 4).

opti-SE greatly improves the simulated SIC, with normalized SIC errors remaining near 1.0 throughout the year (black line in Figure 4). However, the notable SIC errors persist from May to June, and the sharp October increase in errors remain unmitigated. By jointly optimizing the model parameters, opti-SPE further reduces the SIC errors; in particular, the errors from May to June and during October are reduced to acceptable levels (black line with filled circles in Figure 4).
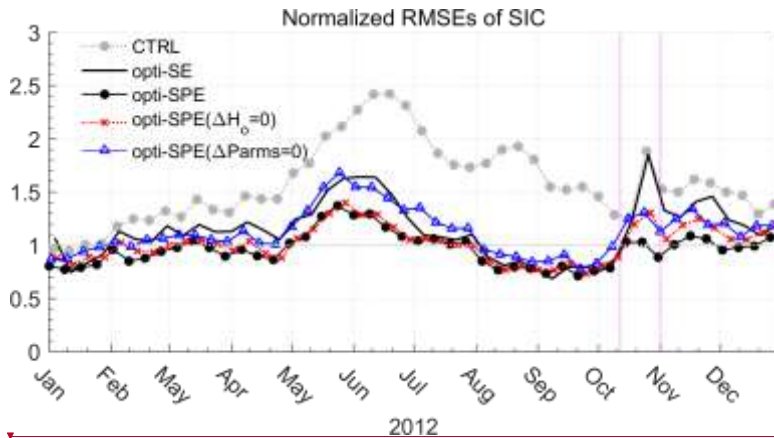
Figure 4. Seasonal evolution of the root mean square errors of SIC (normalized by prior uncertainties) in CTRL, opti-SE, and opti-SPE. In opti-SPE (ΔHo=0), we replace the optimized *Ho* to its default value. And in opti-SPE (ΔParms=0), we reset all the 13 parameters to their default values.

Two additional simulations are presented in Figure 4 to demonstrate the added effects of joint parameter and state estimation. By resetting all the 13 parameters to their default values (opti-SPE(ΔParms=0), blue line with triangles in Figure 4), SIC errors increase to a level similar to that in opti-SE (black line with filled circles in Figure 4). However, in October, the SIC errors are smaller than opti-SE when reset the 13 parameters to their default values. This indicates that the data assimilation finds a smaller minimum of the cost function J which is inaccessible in opti-SE. The further improvements in opti-SPE after October are partially attributed to adjustments to the parameter H_o, as evidenced by the sharp increase in SIC errors when $\Delta H_o=0$ (opti-SPE ($\Delta H_o=0$), dotted red line with crosses in Figure 4).

Since the sea ice recovery process in October impacts ocean-sea ice-atmosphere fluxes and sea ice thickness in subsequent years, we now focus on the SIC improvements during this period. Pronounced SIC differences between the control run and satellite observations appear in the Arctic's Pacific sector (enclosed by the dashed black line in Figure 5a–c), where the most extensive summer sea ice loss occurs across the Arctic Ocean. At the beginning of October, the Arctic's Pacific sector is ice-free (red line with crosses in Figure 5d). The control run fails to reproduce the ice-free conditions (grey line with filled circles in Figure 5d). Both opti-SE and opti-SPE reproduce the ice-free conditions well (black line with triangles and blue line with rectangles in Figure 5d). Starting from October 10, the sea ice begins to recover. Compared with the control run and observations, opti-SE underestimates SIC by more than 40% (Figure 5b), and this underestimation persists until the early November (Figure 5d). By simultaneously adjusting the
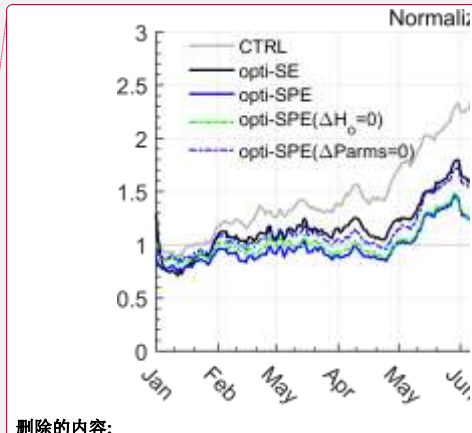
311 model parameters, opti-SPE improves the sea ice recovery process and successfully reduces the negative SIC bias
312 (Figure 5c, d).
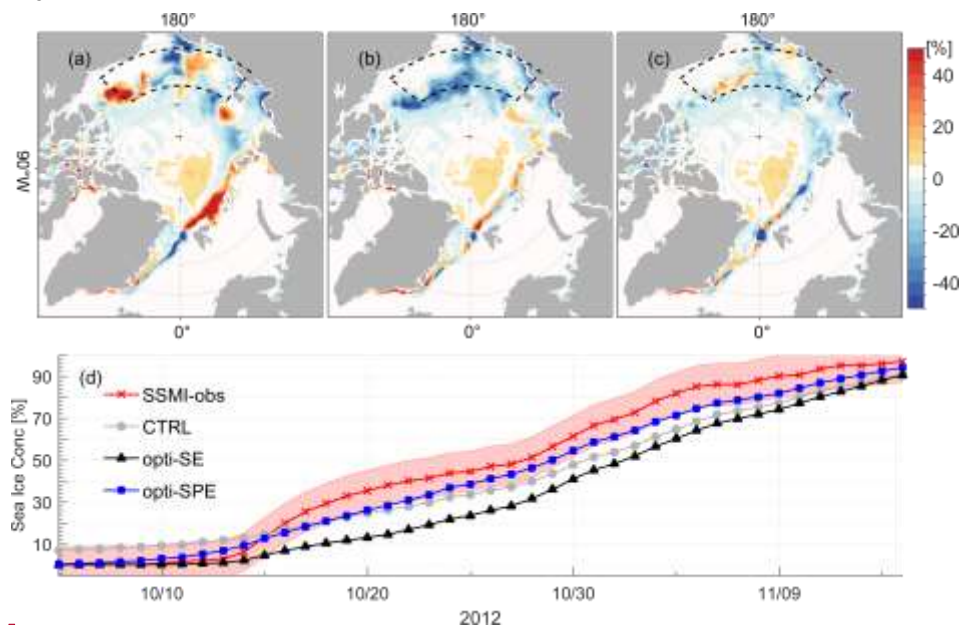
313
314 **Figure 5. Model-data differences of SIC averaged from October 12, 2012 to October 22, 2012 in (a) CTRL, (b) opti-SE,**
315 **and (c) opti-SPE. (d) Temporal evolution of in SIC averaged over the Pacific sector (enclosed by the dashed black line in**
316 **panels (a)–(c)) in the control run (CTRL), two assimilation runs (opti-SE and opti-SPE), and satellite observations (SSMI-**
317 **obs).**
318   During summer, open waters accumulate a large amount of heat, and this ocean heat must be released before the
319 ocean surface refreezes. Since the control run fails to reproduce the ice-free conditions (Figure 5d), more sea ice
320 persists in the Arctic's Pacific sector and less ocean heat is released before the open waters freeze. However, due to
321 the ice-free conditions in the summer season in opti-SE and opti-SPE, the ocean needs to release more heat before
322 refreezing. Therefore, opti-SE initially shows a much slower sea ice growth rate while opti-SPE improves the SIC
323 evolution by adjusting the parameter H_o. In the sea ice model, H_o is the minimum SIT formed in open water, which
324 impacts the vertical and lateral growth of the sea ice and is set to 0.5 m by default. Over the ice-free water, decreasing
325 H_o reduces the amount of latent heat that needs to be released during the initial formation process of sea ice. After
326 initial formation, the decreased H_o accelerates the formation of thinner sea ice in open areas. In opti-SPE, H_o is reduced
327 by more than 0.1 m over open water (Figure 6a) at the onset of refreezing (Figure 6b), which gives rise to the rapid
328 growth of thinner sea ice. The accelerated sea ice recovery significantly reduces the heat and momentum exchanges
329 between atmosphere and ocean, altering the feedback processes in the atmosphere-sea ice-ocean system.
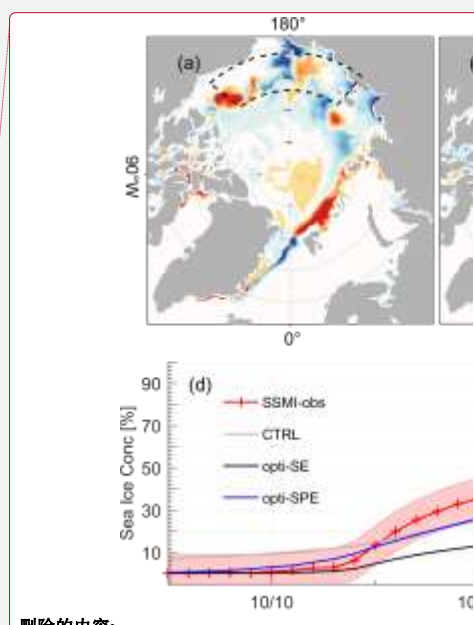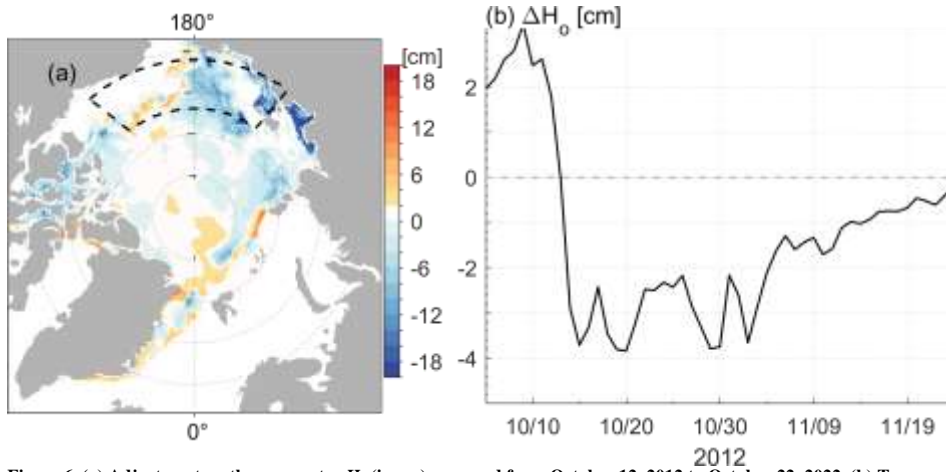
331
332 **Figure 6. (a) Adjustment on the parameter H_o (in cm) averaged from October 12, 2012 to October 22, 2022. (b) Temporal**
333 **changes in adjustments of H_o averaged over the Arctic's Pacific sector (enclosed by the dashed black line in (a)).**

334 **4.3 Comparisons against Independent Observations**

335 **4.3.1 Measurements at BGEP Moorings**

336   In this subsection, we interpolated the gridded SIC and SIT data to the BGEP mooring locations to explore their
337 seasonal variations.

338   The sea ice extent in 2012 reached the unprecedentedly low values since the satellite era. The ULSs of three
339 moorings observed ice-free conditions from August to October. The control run fails to simulate the ice-free conditions,
340 while both opti-SE and opti-SPE successfully reproduce the seasonal SIC variation (Figures 7a−c). opti-SPE shows
341 smaller RMSE at M_b and M_d than opti-SE and CTRL (see the numbers in Figure 7b, c). In opti-SPE, a pack ice broke
342 off from the main ice field from July 20 to early August and gradually melted at M_a, resulting in slightly larger RMSEs
343 (Figure 7a).

344   For SIT, the two assimilation runs bring the simulated SIT into consistency with the CS2SMOS observations
345 (Figure 7d−f) and ULS-measurements. From January to August, the gridded SIT (the CS2SMOS data and the two
346 assimilation runs) agrees well with the ULS-measured SIT, as the Beaufort Sea is covered by compact ice. However,
347 from October to December, when the ocean starts to freeze, systematic discrepancies emerge between the CS2SMOS,
348 the two assimilation runs, and the ULS-measurements: SIT increases more rapidly in the CS2SMOS dataset than in
349 either two assimilation runs or the ULS-measurements. Overall, the two assimilation runs exhibit the smallest errors
350 against the ULS-observed SIT and satellite-observed SIC, within the prior observational errors.
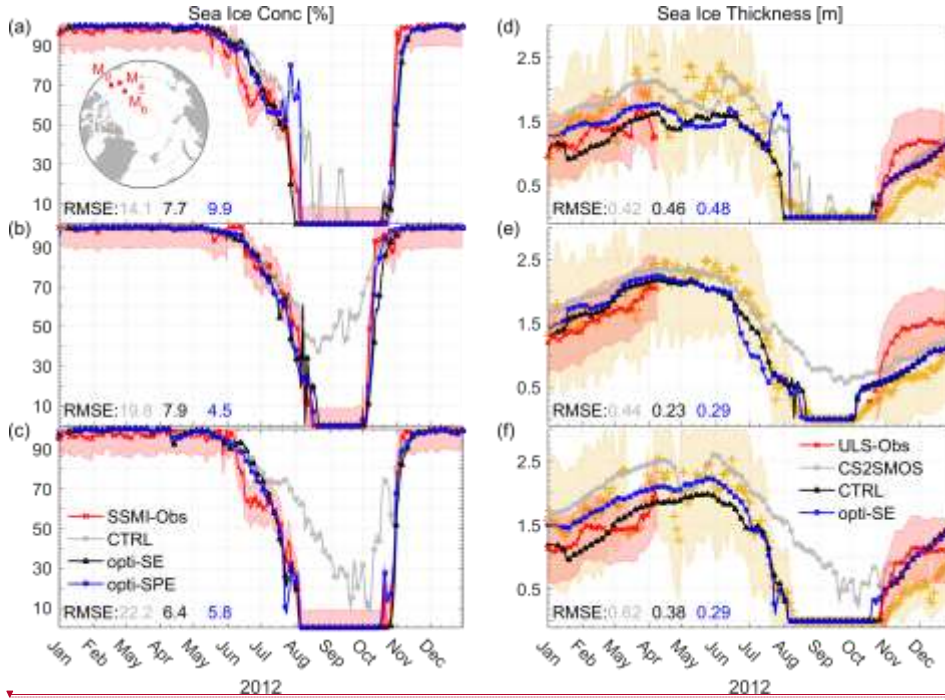
Figure 7. SIC from satellite observations (SSMI-Obs), CTRL, opti-SE and opti-SPE at the mooring locations (a) Ma, (b) Mb, and (c) Md (see locations in subplot of panel (a)). The RMSEs of SIC between the three simulations and SSMI-Obs are listed in panels (a)‒(c). Panels (d)-(f) are the corresponding SIT derived from the upward looking sonar (ULS-Obs), CS2SMOS, CTRL, opti-SE, and opti-SPE. And the RMSEs of SIT between the three simulations and ULS-Obs are also listed in panels (d)‒(f). The shadings indicate the uncertainties of SIC and SIT obervations. For the ULS-Obs, we use the standard deviation of sub-daily sea ice thickness to represent the uncertainties.

4.3.2 SIT from IMB data

The IMBs measure the variation of SIT along the drift trajectories. Comparing these Lagrangian SIT observations with gridded SIT from the sea ice-ocean coupled model and satellite data is challenging, as such comparisons are often subject to biases (e.g., Mu et al., 2018). We use two validation metrics: 1) the mean SIT over the observation time; 2) central root mean square deviation (CRMSD), computed as $\sqrt{\frac{1}{N}\sum_1^N\left((x_n - \overline{x_n}) - (y_n - \overline{y_n})\right)^2}$, where x and y represent the simulated- and measured-SIT, respectively, and the overbar denotes time average. N denotes the total number of valid SIT observations from an IMB, and n represents the index of individual observations. Smaller CRMSD values indicate better agreement between simulations and observations in capturing sea ice evolution. We selected six IMBs with long records: one deployed in 2011 in the central Beaufort Sea (2011J), which drifted toward the Chukchi Sea (top left panel in Figure 8) in 2012; the remaining five IMBs were deployed in 2012 in the central Arctic.
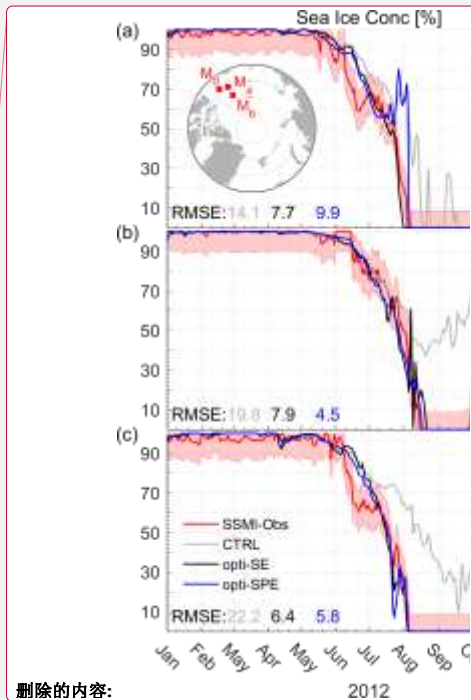
删除的内容:
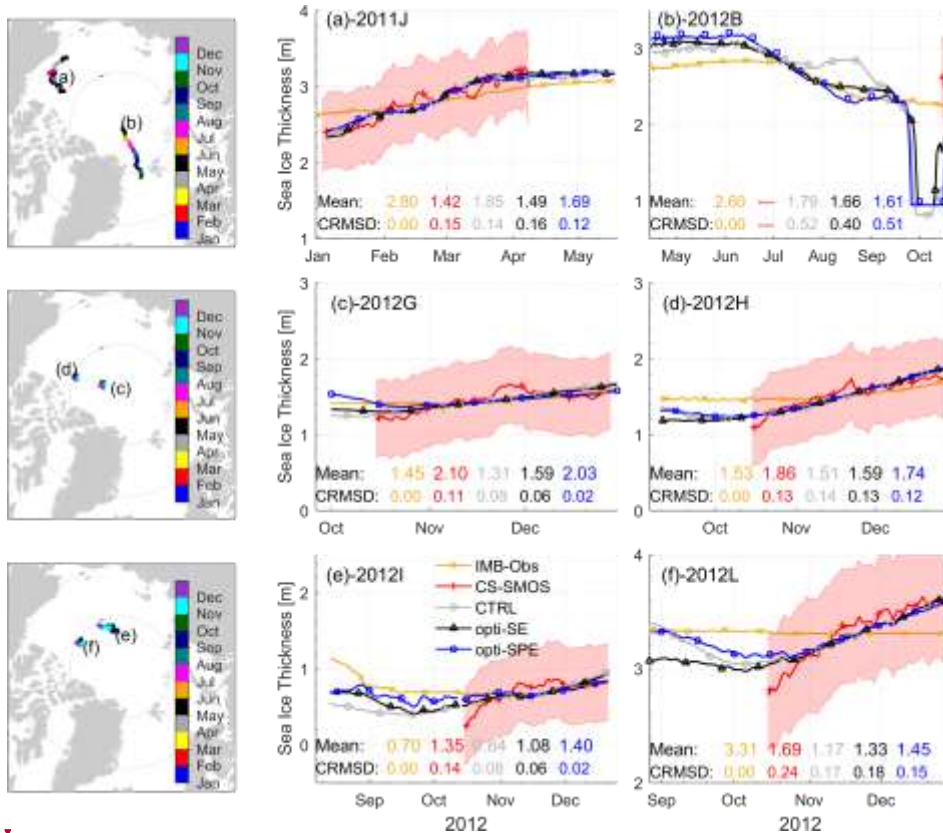
369
370 **Figure 8. SIT along the IMB trajectories. The IMB trajectories (a-2011J, b-2012B, c-2012G, d-2012H, e-2012I, f-2012L) are**
371 **shown in the left panels and the colors indicate the observing time. The SIT of IMBs (yellow lines with crosses), CS2SMOS**
372 **(red lines with plug signs), CTRL (grey lines with circles), opti-SE (black lines with triangles), opti-SPE (blue lines with**
373 **rectangles) are plotted in the right-hand side against observing time. The shadings indicate the CS2SMOS observational**
374 **uncertainties. The statistics (mean SIT and CRMSD against IMBs) of IMBs, CS2SMOS, CTRL, opti-SE, and opti-SPE are**
375 **also shown in each plot.**

376

377   As the mean SIT values indicate, SIT biases of 0.2–0.7 m exist between the CS2SMOS data and the control run

378 (see "Mean" values in Figure 8c–f). The optimization brings the model simulations closer to the CS2SMOS data,

379 especially in opti-SPE. When considering the SIT evolution along the drift trajectories, both opti-SPE and opti-SE

380 effectively reproduce the satellite-measured sea ice growth processes.

381   As expected, IMB measurements typically show 0.5–1.5 m differences compared with CS2SMOS observations

382 ("Mean" values in Figure 8). This likely reflects that the ice conditions at the IMB deployment sites do not necessarily

383 represent a large spatial average, especially for SIT. Considering the SIT variation along the drift trajectories, all the

384 three model simulations and the IMB measurements exhibit much weaker SIT variability than the CS2SMOS

385 observations. This discrepancy arises from the following factors: 1) the buoys are generally deployed on the relatively
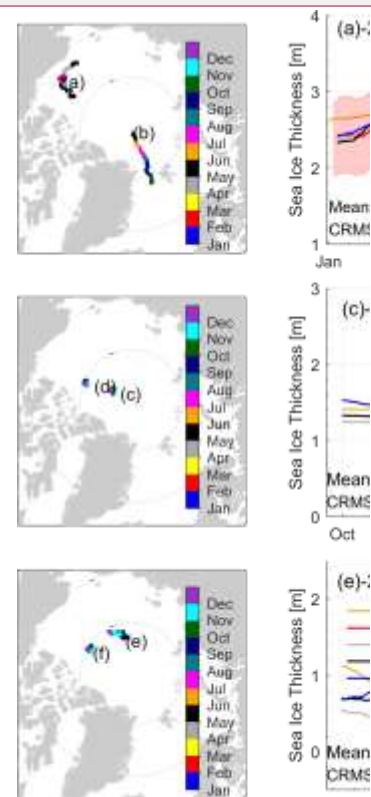
387 thick level ice (Richter-Menge et al., 2006), and 2) the satellite altimeter observations contain significant signals from
388 thin ice, which has a relatively large growth rate (Lei et al., 2022), and ice dynamic deformation can also contribute
389 to the thickening of sea ice within the grid cells (von Albedyll et al., 2022). The CRMSDs, computed between gridded
390 SIT and IMB measurements, indicate that the SIT variations in opti-SPE matches the IMB measurement best.

391   In summary, opti-SPE effectively reduces the mean SIT biases between CS2SMOS observations and the control
392 run. The two assimilation runs reproduce the SIT variation observed by IMBs, with CS2SMOS observations exhibiting
393 greater variability than IMB measurements. Analysis of the CRMSDs reveals that opti-SPE best matches the sea ice
394 evolution as measured by IMBs. We note that data from point measurements of IMBs also have inherent limitations,
395 including the representativeness of initial ice thickness at the deployment, the influence of spatial heterogeneity of
396 snow accumulation during the later measurement stages, and the inability to account for sea ice thickening driven by
397 ice dynamic deformation.

398 **4.5 Sea Ice Velocity from IABP**

399   Twenty-two IABP ice-drifting buoys with drifting periods exceeding 100 days are used to retrieve ice velocities,
400 which are compared against the three model simulations. These buoys were initially deployed on multi-year sea ice
401 and subsequently drifted with the sea ice. Daily sea ice velocities are computed from the buoy locations, and the
402 model-simulated sea ice velocities are interpolated to the buoy locations. We summarize the statistics, including
403 standard deviations, correlation coefficients, and root mean square deviations (RMSDs), using Taylor diagrams
404 (Taylor, 2001).

405   The cost component of SID accounts for 1.45% of the cost function, decreasing slightly to 1.42% in opti-SE and
406 1.43% in opti-SPE. As shown in Figures 9b and 9c, the statistics of CTRL, opti-SE, and opti-SPE with respect to zonal
407 and meridional sea ice velocities from drifting buoys do not differ systematically. Based on the statistics, these buoys
408 can be categorized into two groups: 1) those buoys drifting in regions with compact ice (NOs. 1−14 in Figure 9a); and
409 2) those buoys drifting into regions with gradually decreasing SIC (NOs. 15−22 in Figure 9a).

410   In the first group (Nos. 1−14 in Figure 9a), the RMSEs (0.0429, 0.0417, 0.0423) and correlation coefficients
411 (0.8226, 0.8232, 0.8229) of CTRL, opti-SE, and opti-SPE are comparable. For individual buoys, their statistics in the
412 Taylor diagrams (Figure 9b, c) are also very similar across CTRL, opti-SE, and opti-SPE, with most RMSEs smaller
413 than the prior uncertainties (0.06 m s^{-1}).

414   In contrast to the first group, simulated ice velocities match the buoy observations (NOs. 15−22 in Figure 9a) much
415 less well in the second group, with RMSEs of 0.0880, 0.0973, and 0.0959, and correlation coefficients of 0.5691,
416 0.4863, and 0.4911 for CTRL, opti-SE, and opti-SPE, respectively. Additionally, the statistics of the second groups
417 in the Taylor diagrams are more dispersed, indicating that the two assimilation runs increase the sea ice velocity errors
418 and degrade correlations.
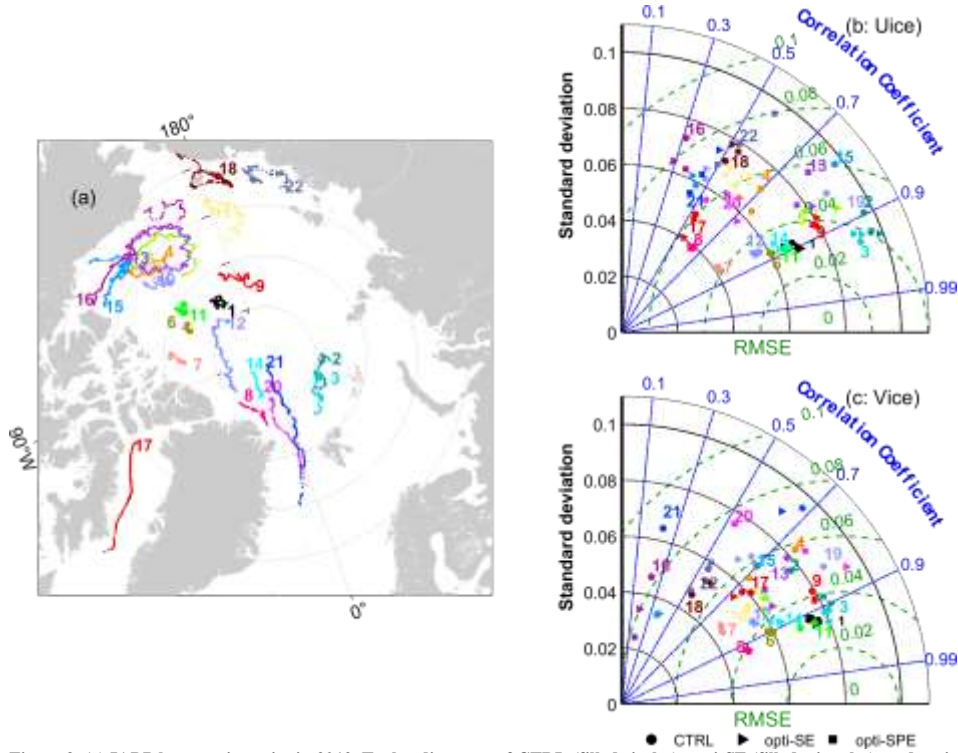
419
420 **Figure 9. (a) IABP buoy trajectories in 2012. Taylor diagrams of CTRL (filled circles), opti-SE (filled triangles), and opti-**
421 **SPE (filled squares) with respect to the (b) zonal (UICE) and (c) meridional (VICE) ice velocities retrieved from the IABP**
422 **buoys.**
423

424   In Figure 10, we further analyze two representative buoys (NOs. 16 and 21 in Figure 9a) that gradually drifted

425 toward the ice edge. The buoy-16 was deployed on April 12, 2012 in the southeastern Beaufort Sea (72.38 °N, -

426 127.47 °E). It drifted westward along the southern periphery of the Beaufort Gyre and ceased data reporting by

427 November 10, 2012 near the Alaska coast (71.34 °N, -160.55 °E). The buoy-21 was deployed on April 15, 2012 in the

428 central Arctic Ocean. It was advected along the transpolar stream, exited through the Fram Strait, and finally ceased

429 data reporting on November 6, 2012 in the Greenland Sea.

430   The sea ice velocity differences are very small in regions with compact ice, as ice internal stress dampens the

431 response of ice motion to wind forcing. When SIC decreases below 85% (Figure 10a, c), the marginal ice zone begins.

432 Ice internal stress weakens and plays a negligible role in sea ice drift. Consequently, sea ice becomes more sensitive

433 to wind stress (Figure 10b, d). In the marginal ice zone, the three model simulations cannot perfectly reproduce the

434 weakening ice field given current sea ice model physics, leading to noticeable errors in sea ice velocities. Along the

435 buoy-16's trajectory, the satellite-observed SIC approached zero by early August (Figure 10a), yet the buoy continued

436 drifting until late October (Figure 10b). The fragmented ice floes likely entered a fully free-drift state, where the ratio

437 of sea ice speed to wind speed reaches a maximum (e.g., Zhang et al., 2022). We suspect that the size of the ice floe

438 carrying the buoy was too small to be captured by the satellite and simulated by the numerical model which has a
439 resolution of ~10 km. This sea ice condition increases comparison uncertainty. Therefore, numerical simulation of sea
440 ice and characterization of heat and momentum exchange between the atmosphere and ocean are extremely
441 challenging in the marginal ice zone.
442
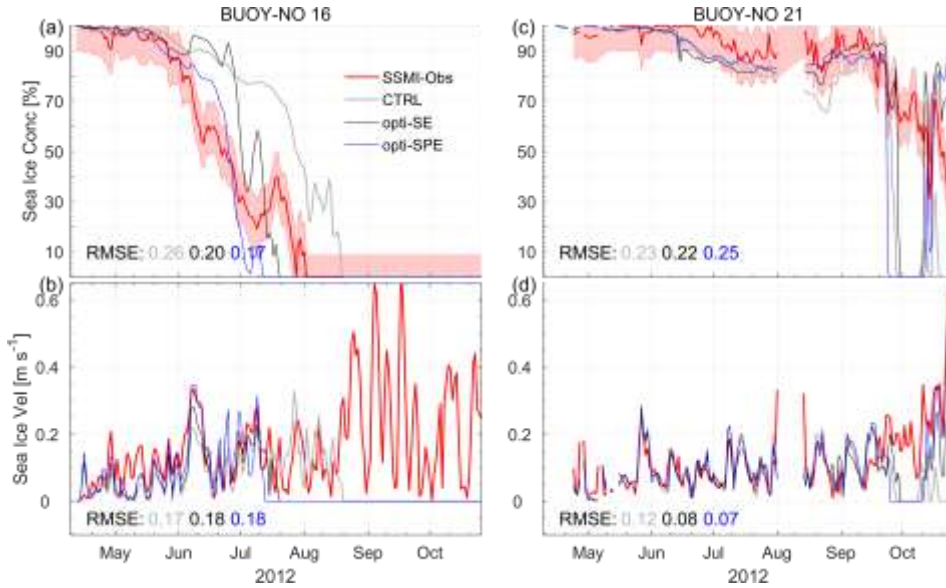
443
444 **Figure 10. Changes in (a, c) SIC and (b, d) sea ice velocity along the buoy trajectories (NOs. 16 and 21 in Figure 9a).**

445 **5 Conclusions and Discussion**

446 Building on the framework of the ECCO project, specifically the work of Fenty et al. (2013) and Lyu et al. (2023),
447 we developed a simultaneous state and parameter estimation scheme for an ocean-sea ice coupled model. To our
448 knowledge, this is the first study to optimize spatiotemporally varying sea ice model parameters together with
449 atmospheric forcing and model initial conditions. By assimilating Arctic ocean and sea ice observations from 2012,
450 we investigated the added effects of the simultaneous state and parameter estimation scheme (opti-SPE) relative to
451 the traditional state estimation scheme (opti-SE) and the free model simulation (CTRL).

452 The results show that opti-SPE further reduces the cost function by 10.5%, with notable improvements in SIC.
453 In both the control run and opti-SE, sea ice grows much slower in the Arctic's Pacific sector in October. By reducing
454 the lead closing parameter H_o (on the order of 0.1 m), opti-SPE accelerates sea ice growth. The lead closing parameters
455 are widely used in Arctic sea ice-ocean assimilation models (Lindsay et al., 2006; Mu et al., 2018; Nguyen et al.,
456 2021), and impact on the sea ice growth process in autumn. Our results suggest that delicate optimization of this
457 parameter is necessary for better simulating Arctic sea ice changes and ocean-sea ice-atmosphere exchanges in the
458 autumn.

459   For SIT, both opti-SE and opti-SPE bring the simulated SIT into agreement with CS2CMOS SIT, taking into
460   account its prior uncertainties. Compared with the independent ULS-measured SIT at BGEP moorings, both
461   assimilation runs efficiently reproduce the seasonal sea ice evolution. The differences between the assimilation runs
462   and the ULS measurements are much smaller than those between CS2SMOS data and ULS measurements, especially
463   from October to December. Considering sea ice evolutions along the six IMB trajectories, opti-SPE performs slightly
464   better than opti-SE. However, the robustness of these comparisons may be limited by the small number of IMBs and
465   their spatial representativeness relative to their surrounding areas.

466   The overall improvements in sea ice velocities from data assimilation are not significant. In regions with compact
467   ice, the two assimilation runs slightly improve the simulated sea ice velocities. However, as buoys drift into the
468   marginal ice zone or near-ice-free regions, both model simulations and the satellite data may fail to simulate or detect
469   small ice floes, resulting in large deviations between the simulated and observed sea ice velocity.

470   Despite using a relatively low-complexity sea ice model compared to the modern sea ice models such as the Los
471   Alamos sea ice model (CICE; Hunke et al., 2020), our assimilation results demonstrate that the model simulations are
472   efficiently brought into agreement with the satellite observations and independent observations. Zampieri et al. (2021)
473   demonstrated that the low-complex sea ice model can be optimized more efficiently, and the overall performance after
474   optimization is largely in line with complex CICE configurations. Therefore, our sea ice model remains a suitable tool
475   for Arctic ocean and sea ice assimilation studies. However, in the next stage, we will update the sea ice module with
476   the more complex CICE model.

477   This study demonstrates that the simultaneous optimization of model parameters and state variables is promising
478   and merits testing with the other assimilation methods (e.g., ensemble Kalman Filters). However, given that the
479   optimal set of sea ice parameters may evolve alongside the thinning of Arctic sea ice, the parameters optimized using
480   2012 observations may not necessarily improve model simulation for the other years. To address this, we plan to
481   assimilate observations spanning the satellite era (1978−2025) and jointly optimize model parameters and state
482   variables. This approach will enable the accurate reconstruction of historical Arctic ocean and sea ice changes, thereby
483   supporting research on Arctic ocean and sea ice variability and trends.

Competing interests

485   The contact author has declared that none of the authors has any competing interests.

Acknowledgments

487   We thank François Massonnet from Universite catholique de Louvain and another anonymous for their constructive
488   and insightful comments on the manuscript. This research has been supported by the National Natural Science
489   Foundation of China (grant No. 42325604), the National Key Research and Development Program of China (grant
490   No. 2021YFC2803304), Program of Shanghai Academic/Technology Research Leader (Grant No. 22XD1403600),
491   and the Southern Marine Science and Engineering Guangdong Laboratory (Zhuhai) (Grant No. ML2023SP219). For
492   the assimilated sea ice variables, we thank the Alfred Wegener Institute, and EUMETSAT Ocean and Sea Ice Satellite
493   Application Facility for supplying the CS2SMOS L4 sea ice thickness, OSI-SAF sea ice concentration and sea ice

删除的内容: errors

删除的内容: in

删除的内容: estimates

删除的内容: .

带格式的: 字体: (默认) Times New Roman, (中文) 宋体, (中文) 中文(中国), 图案: 清除

带格式的: 字体: (默认) Times New Roman, (中文) 宋体, (中文) 中文(中国), 图案: 清除

带格式的: 字体: (默认) Times New Roman, (中文) 宋体, (中文) 中文(中国), 图案: 清除

带格式的: 字体: (默认) Times New Roman, (中文) 宋体, (中文) 中文(中国), 图案: 清除

删除的内容: However, in the next stage, we will update the sea ice module with the more complex CICE model and reconstruct Arctic ocean and sea ice changes using SPE.

drift datasets, respectively. For the hydrographic observations, we acknowledge the Met Office, the Copernicus Marine Service, and the remoting sensing system for archiving and sharing the EN4, the along-track SLA, and sea surface temperature datasets. For the independent observations, we thank the Woods Hole Oceanographic Institution for the sea ice draft measured by the ULS, the Cold Regions Research and Engineering Laboratory-Dartmouth Mass Balance Buoy Program for the IMB data, the University of Washington for the buoy drifting trajectories.

Author contribution

Conceptualization: GL, AK, and LM. Experiments design and results analysis: GL. Investigation: RL, XL, and CL.

Original draft: GL. Review and editing: GL, LM, AK, RL, XL, and CL.

Open Research

Code and Data Availability Statement

The sea ice-ocean coupled model is based on MITgcm_c63m(https://mitgcm.org/download/other_checkpoints/). The modified MITgcm (c63m) codes are available to the public on Zenodo at https://doi.org/10.5281/zenodo.14584929 (Lyu et al., 2025). The sea ice variables and model parameters from the control run and the two assimilation runs are available on Zenodo at https://doi.org/10.5281/zenodo.14584780 (Lyu, 2025). We note that a commercial TAF license is required to fully reproduce the optimization steps described in this study.

All the assimilated and independent validation are publicly available. The following datasets were provided with DOI numbers: the global ocean along track L3 sea surface heights can be downloaded from the E.U. Copernicus Marine Service Information (https://doi.org/10.48670/moi-00146); the sea ice concentration and drift data were based on the EUMETSAT OSI-450-a (doi:10.15770/EUM_SAF_OSI_0013), and osi-405-c (doi:10.15770/EUM_SAF_OSI_NRT_2007); the CryoSat-SMOS merged sea ice thickness data (https://doi.org/10.57780/sm1-4f787c3, European Space Agency., 2023) is available at https://spaces.awi.de/display/CS2SMOS/CryoSat-SMOS+Merged+Sea+Ice+Thickness.

The following datasets don't have DOI numbers, we provide their accessable links: the sea surface temperature were retrived from https://data.remss.com/SST/daily/mw_ir/v05.1/netcdf/ (last access: 13 April 2025, Gentemann et al., 1994); the EN.4.2.2 data were obtained from https://www.metoffice.gov.uk/hadobs/en4/ (last access: 13 April 2025, Good et al., 2013) and are ©British Crown Copyright, Met Office, 2013, provided under a Non-Commercial Government Licence http://www.nationalarchives.gov.uk/doc/non-commercial-government-licence/version/2/ (last access:13 April 2025); the WOA18 climatological temperature and salinity data were download form https://www.ncei.noaa.gov/access/world-ocean-atlas-2018/ (last access, 13 April 2025, Locarnini et al., 2018; Zweng et al., 2018); the ULS-measured ice drafts were collected and shared by the Beaufort Gyre Exploration Program based at the Woods Hole Oceanographic Institution (https://www2.whoi.edu/site/beaufortgyre/data/mooring-data/, last access: 13 April 2025) in collaboration with researchers from Fisheries and Oceans Canada at the Institute of Ocean Sciences; the IMB-measured sea ice thickness were from http://imb-crrel-dartmouth.org/results/ (Perovich et al., 2025,

536   last access: 13 April 2025); the sea ice drift trajecties were collected by the International Arctic Buoy Programme at

537   https://iabp.apl.uw.edu/data.html (last access: 13 April 2025).

538

539 **References**

540 Annan, J. D., Hargreaves, J. C., Edwards, N. R., & Marsh, R. (2005). Parameter estimation in an intermediate
541   complexity earth system model using an ensemble Kalman filter. *Ocean Modelling*, *8*(1), 135-154.
542   https://doi.org/https://doi.org/10.1016/j.ocemod.2003.12.004
543 Branstator, G., & Teng, H. (2010). Two Limits of Initial-Value Decadal Predictability in a CGCM. *Journal of
544   Climate*, *23*(23), 6292-6311. https://doi.org/https://doi.org/10.1175/2010JCLI3678.1
545 Bretherton, C. S., Henn, B., Kwa, A., Brenowitz, N. D., Watt-Meyer, O., McGibbon, J., Perkins, W. A., Clark, S. K.,
546   & Harris, L. (2022). Correcting Coarse-Grid Weather and Climate Models by Machine Learning From
547   Global Storm-Resolving Simulations. *Journal of Advances in Modeling Earth Systems*, *14*(2),
548   e2021MS002794. https://doi.org/https://doi.org/10.1029/2021MS002794
549 Chen, Y., Lei, R., Zhao, X., Wu, S., Liu, Y., Fan, P., Ji, Q., Zhang, P., & Pang, X. (2023). A new sea ice
550   concentration product in the polar regions derived from the FengYun-3 MWRI sensors. *Earth Syst. Sci.
551   Data*, *15*(7), 3223-3242. https://doi.org/10.5194/essd-15-3223-2023
552 European Space Agency, 2023, SMOS-CryoSat L4 Sea Ice Thickness, Version 206. https://doi.org/10.57780/sm1-
553   4f787c3
554 Forget, G., Campin, J.-M., Heimbach, P., Hill, C. N., Ponte, R. M., and Wunsch, C. (2015). ECCO version 4: an
555   integrated framework for non-linear inverse modeling and global ocean state estimation, *Geosci. Model Dev.,*
556   8, 3071–3104, https://doi.org/10.5194/gmd-8-3071-2015.
557 Fenty, I., & Heimbach, P. (2013). Coupled Sea Ice–Ocean-State Estimation in the Labrador Sea and Baffin Bay.
558   *Journal of Physical Oceanography*, *43*(5), 884-904. https://doi.org/https://doi.org/10.1175/JPO-D-12-065.1
559 Fenty, I., Menemenlis, D., & Zhang, H. (2017). Global coupled sea ice-ocean state estimation. *Climate Dynamics*,
560   *49*(3), 931-956. https://doi.org/10.1007/s00382-015-2796-6
561 Gentemann, C. L., Wentz, F. J., Mears, C. A., & Smith, D. K. (2004). In situ validation of Tropical Rainfall
562   Measuring Mission microwave sea surface temperatures. *Journal of Geophysical Research: Oceans*,
563   *109*(C4). https://doi.org/https://doi.org/10.1029/2003JC002092
564 Giering, R., & Kaminski, T. (1998). Recipes for adjoint code construction. *ACM Transactions on Mathematical
565   Software (TOMS)*, *24*(4), 437-474.
566 Gilbert, J. C., & Lemaréchal, C. (2006). The module M1QN3.
567 Good, S. A., Martin, M. J., & Rayner, N. A. (2013). EN4: Quality controlled ocean temperature and salinity profiles
568   and monthly objective analyses with uncertainty estimates. *Journal of Geophysical Research: Oceans*,
569   *118*(12), 6704-6716. https://doi.org/10.1002/2013jc009067
570 Heimbach, P., Menemenlis, D., Losch, M., Campin, J.-M., & Hill, C. (2010). On the formulation of sea-ice models.
571   Part 2: Lessons from multi-year adjoint sea-ice export sensitivities through the Canadian Arctic
572   Archipelago. *Ocean Modelling*, *33*(1), 145-158.
573   https://doi.org/https://doi.org/10.1016/j.ocemod.2010.02.002
574 Hibler, W. (1979). A Dynamic Thermodynamic Sea Ice Model. *Journal of Physical Oceanography*, *9*(4), 815-846.
575   https://doi.org/10.1175/1520-0485(1979)009<0815:adtsim>2.0.co;2
576 Hibler , W. (1980). Modeling a Variable Thickness Sea Ice Cover. *Monthly Weather Review*, *108*(12), 1943-1973.
577   https://doi.org/10.1175/1520-0493(1980)108<1943:mavtsi>2.0.co;2
578 Horvat, C., & Roach, L. A. (2022). WIFF1.0: a hybrid machine-learning-based parameterization of wave-induced
579   sea ice floe fracture. *Geosci. Model Dev.*, *15*(2), 803-814. https://doi.org/10.5194/gmd-15-803-2022
580 Hourdin, F., Mauritsen, T., Gettelman, A., Golaz, J.-C., Balaji, V., Duan, Q., Folini, D., Ji, D., Klocke, D., Qian, Y.,
581   Rauser, F., Rio, C., Tomassini, L., Watanabe, M., & Williamson, D. (2017). The Art and Science of
582   Climate Model Tuning. *Bulletin of the American meteorological Society*, *98*(3), 589-602.
583   https://doi.org/https://doi.org/10.1175/BAMS-D-15-00135.1
584 Hu, X.-M., Zhang, F., & Nielsen-Gammon, J. W. (2010). Ensemble-based simultaneous state and parameter
585   estimation for treatment of mesoscale model error: A real-data study. *Geophysical Research Letters*, *37*(8).
586   https://doi.org/https://doi.org/10.1029/2010GL043017
587 Hunke, E. C., Allard, R., Bailey, D. A., Blain, P., Craig, A., Dupont, F., & Winton, M. (2020a). CICE-
588   Consortium/CICE: CICE version 6.1.2 (version 6.1.2). Zenodo. https://doi.org/10.5281/zenodo.3888653
589 Jackson, C. S., Sen, M. K., Huerta, G., Deng, Y., & Bowman, K. P. (2008). Error Reduction and Convergence in
590   Climate Prediction. *Journal of Climate*, *21*(24), 6698-6709.
591   https://doi.org/https://doi.org/10.1175/2008JCLI2112.1

Kim, J. G., Hunke, E. C., & Lipscomb, W. H. (2006). Sensitivity analysis and parameter tuning scheme for global sea-ice modeling. *Ocean Modelling*, *14*(1), 61-80. https://doi.org/https://doi.org/10.1016/j.ocemod.2006.03.003

Kochkov, D., Yuval, J., Langmore, I., Norgaard, P., Smith, J., Mooers, G., Klöwer, M., Lottes, J., Rasp, S., Düben, P., Hatfield, S., Battaglia, P., Sanchez-Gonzalez, A., Willson, M., Brenner, M. P., & Hoyer, S. (2024). Neural general circulation models for weather and climate. *Nature*, *632*(8027), 1060-1066. https://doi.org/10.1038/s41586-024-07744-y

Koldunov, N. V., Köhl, A., Serra, N., & Stammer, D. (2017). Sea ice assimilation into a coupled ocean–sea ice model using its adjoint. *The Cryosphere*, *11*(5), 2265-2281. https://doi.org/10.5194/tc-11-2265-2017

Koo, Y., Lei, R., Cheng, Y., Cheng, B., Xie, H., Hoppmann, M., Kurtz, N. T., Ackley, S. F., & Mestas-Nuñez, A. M. (2021). Estimation of thermodynamic and dynamic contributions to sea ice growth in the Central Arctic using ICESat-2 and MOSAiC SIMBA buoy data. *Remote Sensing of Environment*, *267*, 112730. https://doi.org/https://doi.org/10.1016/j.rse.2021.112730

Krishfield, R. A., Proshutinsky, A., Tateyama, K., Williams, W. J., Carmack, E. C., McLaughlin, F. A., & Timmermans, M.-L. (2014). Deterioration of perennial sea ice in the Beaufort Gyre from 2003 to 2012 and its impact on the oceanic freshwater cycle. *Journal of Geophysical Research: Oceans*, *119*(2), 1271-1305. https://doi.org/https://doi.org/10.1002/2013JC008999

Lavergne, T., Eastwood, S., Teffah, Z., Schyberg, H., & Breivik, L.-A. (2010). Sea ice motion from low-resolution satellite sensors: An alternative method and its validation in the Arctic. *Journal of Geophysical Research: Oceans*, *115*(C10). https://doi.org/https://doi.org/10.1029/2009JC005958

Lavergne, T., Sørensen, A. M., Kern, S., Tonboe, R., Notz, D., Aaboe, S., Bell, L., Dybkjær, G., Eastwood, S., Gabarro, C., Heygster, G., Killie, M. A., Brandt Kreiner, M., Lavelle, J., Saldo, R., Sandven, S., & Pedersen, L. T. (2019). Version 2 of the EUMETSAT OSI SAF and ESA CCI sea-ice concentration climate data records. *The Cryosphere*, *13*(1), 49-78. https://doi.org/10.5194/tc-13-49-2019

Lei, R., Cheng, B., Hoppmann, M., Zhang, F., Zuo, G., Hutchings, J. K., Lin, L., Lan, M., Wang, H., Regnery, J., Krumpen, T., Haapala, J., Rabe, B., Perovich, D. K., & Nicolaus, M. (2022). Seasonality and timing of sea ice mass balance and heat fluxes in the Arctic transpolar drift during 2019–2020. *Elementa: Science of the Anthropocene*, *10*(1). https://doi.org/10.1525/elementa.2021.000089

Li, Z., Chao, Y., McWilliams, J. C., & Ide, K. (2008). A Three-Dimensional Variational Data Assimilation Scheme for the Regional Ocean Modeling System. *Journal of Atmospheric and Oceanic Technology*, *25*(11), 2074-2090. https://doi.org/https://doi.org/10.1175/2008JTECHO594.1

Lindsay, R. W., & Zhang, J. (2006). Assimilation of Ice Concentration in an Ice–Ocean Model. *Journal of Atmospheric and Oceanic Technology*, *23*(5), 742-749. https://doi.org/10.1175/jtech1871.1

Liu, C., Köhl, A., & Stammer, D. (2012). Adjoint-Based Estimation of Eddy-Induced Tracer Mixing Parameters in the Global Ocean. *Journal of Physical Oceanography*, *42*(7), 1186-1206. https://doi.org/10.1175/jpo-d-11-0162.1

Liu, X., & Zhang, L. (2018). Study on optimization of sea ice concentration with adjoint method. *Journal of Coastal Research, 84*, 44-50

Locarnini, R. A., Mishonov, A. V., Baranova, O. K., Boyer, T. P., Zweng, M. M., Garcia, H. E., Reagan, J. R., Seidov, D., Weathers, K. W., Paver, C. R., & V, S. I. (2018). World Ocean Atlas 2018, Volume 1: Temperature. *Levitus, edited by: Mishonov, A., NOAA Atlas NESDIS*, *82*, 52.

Losch, M., Menemenlis, D., Campin, J.-M., Heimbach, P., & Hill, C. (2010). On the formulation of sea-ice models. Part 1: Effects of different solver implementations and parameterizations. *Ocean Modelling*, *33*(1), 129-144. https://doi.org/https://doi.org/10.1016/j.ocemod.2009.12.008

Lu, Y., Wang, X., & Dong, J. (2021). Melt Pond Scheme Parameter Estimation Using an Adjoint Model. *Advances in Atmospheric Sciences*, *38*(9), 1525-1536. https://doi.org/10.1007/s00376-021-0305-x

Lyu, G., Koehl, A., Serra, N., & Stammer, D. (2021a). Assessing the current and future Arctic Ocean observing system with observing system simulating experiments. *Quarterly Journal of the royal meteorological society*, *147*(738), 2670-2690. https://doi.org/https://doi.org/10.1002/qj.4044

Lyu, G., Koehl, A., Serra, N., Stammer, D., & Xie, J. (2021b). Arctic ocean–sea ice reanalysis for the period 2007–2016 using the adjoint method. *Quarterly Journal of the royal meteorological society*, *147*(736), 1908-1929. https://doi.org/https://doi.org/10.1002/qj.4002

Lyu, G., Koehl, A., Wu, X., Zhou, M., & Stammer, D. (2023). Effects of including the adjoint sea ice rheology on estimating Arctic Ocean–sea ice state. *Ocean Sci.*, *19*(2), 305-319. https://doi.org/10.5194/os-19-305-2023

Lyu, G., Köhl, A., Matei, I., & Stammer, D. (2018). Adjoint-Based Climate Model Tuning: Application to the Planet Simulator. *Journal of Advances in Modeling Earth Systems*, *10*(1), 207-222. https://doi.org/https://doi.org/10.1002/2017MS001194

Lyu, G . (2025). MITgcm model developed for state and parameter estimation in a pan-Arctic ocean and sea ice model. Zenodo. https://doi.org/10.5281/zenodo.14584929

Lyu, G ., Mu, L., Koehl, A., Lei, R., Liang, X., & Liu, C. (2025). MITgcm model developed for state and parameter estimation in a pan-Arctic ocean and sea ice model using MITgcm (c63m) [Data set]. Zenodo. https://doi.org/10.5281/zenodo.14584780

Marshall, J., Adcroft, A., Hill, C., Perelman, L., & Heisey, C. (1997). A finite‐volume, incompressible Navier Stokes model for studies of the ocean on parallel computers. *Journal of Geophysical Research: Oceans*, *102*(C3), 5753-5766.

Massonnet, F., Goosse, H., Fichefet, T., & Counillon, F. (2014). Calibration of sea ice dynamic parameters in an ocean-sea ice model using an ensemble Kalman filter. *Journal of Geophysical Research: Oceans*, *119*(7), 4168-4184. https://doi.org/https://doi.org/10.1002/2013JC009705

Mauritsen, T., Stevens, B., Roeckner, E., Crueger, T., Esch, M., Giorgetta, M., Haak, H., Jungclaus, J., Klocke, D., Matei, D., Mikolajewicz, U., Notz, D., Pincus, R., Schmidt, H., & Tomassini, L. (2012). Tuning the climate of a global model. *Journal of Advances in Modeling Earth Systems*, *4*(3). https://doi.org/https://doi.org/10.1029/2012MS000154

Miller, P. A., Laxon, S. W., & Feltham, D. L. (2005). Improving the spatial distribution of modeled Arctic sea ice thickness. *Geophysical Research Letters*, *32*(18). https://doi.org/https://doi.org/10.1029/2005GL023622

Mu, L., Losch, M., Yang, Q., Ricker, R., Losa, S. N., & Nerger, L. (2018). Arctic-Wide Sea Ice Thickness Estimates From Combining Satellite Remote Sensing Data and a Dynamic Ice-Ocean Model with Data Assimilation During the CryoSat-2 Period. *Journal of Geophysical Research: Oceans*, *123*(11), 7763-7780. https://doi.org/https://doi.org/10.1029/2018JC014316

Murphy, J. M., Sexton, D. M. H., Barnett, D. N., Jones, G. S., Webb, M. J., Collins, M., & Stainforth, D. A. (2004). Quantification of modelling uncertainties in a large ensemble of climate change simulations. *Nature*, *430*(7001), 768-772. https://doi.org/10.1038/nature02771

Nie, Y., Li, C., Vancoppenolle, M., Cheng, B., Boeira Dias, F., Lv, X., & Uotila, P. (2022). Sensitivity of NEMO4.0-SI3 model parameters on sea ice budgets in the Southern Ocean. *Geosci. Model Dev., 16*, 1395-1425. https://doi.org/10.5194/gmd-16-1395-2023

Nguyen, A. T., Menemenlis, D., & Kwok, R. (2011). Arctic ice-ocean simulation with optimized model parameters: Approach and assessment. *Journal of Geophysical Research: Oceans*, *116*(C4). https://doi.org/https://doi.org/10.1029/2010JC006573

Nguyen, A. T., Pillar, H., Ocaña, V., Bigdeli, A., Smith, T. A., & Heimbach, P. (2021). The Arctic Subpolar Gyre sTate Estimate: Description and Assessment of a Data-Constrained, Dynamically Consistent Ocean-Sea Ice Estimate for 2002–2017. *Journal of Advances in Modeling Earth Systems*, *13*(5), e2020MS002398. https://doi.org/https://doi.org/10.1029/2020MS002398

Panteleev, G., Yaremchuk, M., Stroh, J. N., Francis, O. P., & Allard, R. (2020). Parameter optimization in sea ice models with elastic–viscoplastic rheology. *The Cryosphere*, *14*(12), 4427-4451. https://doi.org/10.5194/tc-14-4427-2020

Perovich, D., J. Richter-Menge, and C. Polashenski, Observing and understanding climate change: Monitoring the mass balance, motion, and thickness of Arctic sea ice, http://imb-crrel-dartmouth.org , 2025.

Pujol, M. I., Faugère, Y., Taburet, G., Dupuy, S., Pelloquin, C., Ablain, M., & Picot, N. (2016). DUACS DT2014: the new multi-mission altimeter data set reprocessed over 20 years. *Ocean Sci.*, *12*(5), 1067-1090. https://doi.org/10.5194/os-12-1067-2016

Richter-Menge, J. A., Perovich, D. K., Elder, B. C., Claffey, K., Rigor, I., & Ortmeyer, M. (2006). Ice mass-balance buoys: a tool for measuring and attributing changes in the thickness of the Arctic sea-ice cover. *Annals of Glaciology*, *44*, 205-210. https://doi.org/10.3189/172756406781811727

Ricker, R., Hendricks, S., Kaleschke, L., Tian-Kunze, X., King, J., & Haas, C. (2017). A weekly Arctic sea-ice thickness data record from merged CryoSat-2 and SMOS satellite data. *The Cryosphere*, *11*(4), 1607-1623. https://doi.org/10.5194/tc-11-1607-2017

Sumata, H., Kauker, F., Karcher, M., & Gerdes, R. (2019). Simultaneous Parameter Optimization of an Arctic Sea Ice–Ocean Model by a Genetic Algorithm. *Monthly Weather Review*, *147*(6), 1899-1926. https://doi.org/10.1175/mwr-d-18-0360.1

Taburet, G., Sanchez-Roman, A., Ballarotta, M., Pujol, M. I., Legeais, J. F., Fournier, F., Faugere, Y., & Dibarboure, G. (2019). DUACS DT2018: 25 years of reprocessed sea level altimetry products. *Ocean Sci.*, *15*(5), 1207-1224. https://doi.org/10.5194/os-15-1207-2019

Taylor, K. E. (2001). Summarizing multiple aspects of model performance in a single diagram. *Journal of Geophysical Research: Atmospheres*, *106*(D7), 7183-7192.

Uotila, P., O'Farrell, S., Marsland, S. J., & Bi, D. (2012). A sea-ice sensitivity study with a global ocean-ice model. *Ocean Modelling*, *51*, 1-18. https://doi.org/https://doi.org/10.1016/j.ocemod.2012.04.002

von Albedyll, L., Hendricks, S., Grodofzig, R., Krumpen, T., Arndt, S., Belter, H. J., Birnbaum, G., Cheng, B., Hoppmann, M., Hutchings, J., Itkin, P., Lei, R., Nicolaus, M., Ricker, R., Rohde, J., Suhrhoff, M., Timofeeva, A., Watkins, D., Webster, M., & Haas, C. (2022). Thermodynamic and dynamic contributions to seasonal Arctic sea ice thickness distributions from airborne observations. *Elementa: Science of the Anthropocene*, *10*(1). https://doi.org/10.1525/elementa.2021.00074

Weaver, A. T., & Mirouze, I. (2013). On the diffusion equation and its application to isotropic and anisotropic correlation modelling in variational assimilation. *Quarterly Journal of the Royal Meteorological Society*, *139*(670), 242-260. https://doi.org/https://doi.org/10.1002/qj.1955

Williamson, D., Goldstein, M., Allison, L., Blaker, A., Challenor, P., Jackson, L., & Yamazaki, K. (2013). History matching for exploring and reducing climate model parameter space using observations and a large perturbed physics ensemble. *Climate Dynamics*, *41*(7), 1703-1729. https://doi.org/10.1007/s00382-013-1896-4

Wu, X., Zhang, S., Liu, Z., Rosati, A., Delworth, T. L., & Liu, Y. (2012). Impact of Geographic-Dependent Parameter Optimization on Climate Estimation and Prediction: Simulation with an Intermediate Coupled Model. *Monthly Weather Review*, *140*(12), 3956-3971. https://doi.org/https://doi.org/10.1175/MWR-D-11-00298.1

Yang, B., Qian, Y., Lin, G., Leung, L. R., Rasch, P. J., Zhang, G. J., McFarlane, S. A., Zhao, C., Zhang, Y., Wang, H., Wang, M., & Liu, X. (2013). Uncertainty quantification and parameter tuning in the CAM5 Zhang-McFarlane convection scheme and impact of improved convection on the global circulation and climate. *Journal of Geophysical Research: Atmospheres*, *118*(2), 395-415. https://doi.org/https://doi.org/10.1029/2012JD018213

Zampieri, L., Kauker, F., Fröhle, J., Sumata, H., Hunke, E. C., & Goessling, H. F. (2021). Impact of Sea-Ice Model Complexity on the Performance of an Unstructured-Mesh Sea-Ice/Ocean Model under Different Atmospheric Forcings. *Journal of Advances in Modeling Earth Systems*, *13*(5), e2020MS002438. https://doi.org/https://doi.org/10.1029/2020MS002438

Zhang, F., Pang, X., Lei, R., Zhai, M., Zhao, X., & Cai, Q. (2022). Arctic sea ice motion change and response to atmospheric forcing between 1979 and 2019. *International Journal of Climatology*, *42*(3), 1854-1876. https://doi.org/https://doi.org/10.1002/joc.7340

Zhang, J., & Hibler , W. (1997). On an efficient numerical method for modeling sea ice dynamics. *Journal of Geophysical Research: Oceans*, *102*(C4), 8691-8702.

Zhang, S. (2011). A Study of Impacts of Coupled Model Initial Shocks and State–Parameter Optimization on Climate Predictions Using a Simple Pycnocline Prediction Model. *Journal of Climate*, *24*(23), 6210-6226. https://doi.org/https://doi.org/10.1175/JCLI-D-10-05003.1

Zweng, M. M., Reagan, J. R., Seidov, D., Boyer, T. P., Locarnini, R. A., Garcia, H. E., Mishonov, A. V., Baranova, O. K., Weathers, K. W., Paver, C. R., & V, S. I. (2018). World Ocean Atlas 2018, Volume 2: Salinity. *Levitus, edited by: Mishonov, A., NOAA Atlas NESDIS*, *82*, 50.